

Position Control of Linear Switched Reluctance Motors for High-Precision Applications

Wai-Chuen Gan, *Member, IEEE*, Norbert C. Cheung, *Member, IEEE*, and Li Qiu, *Senior Member, IEEE*

Abstract—Most advanced manufacturing processes require precise motions for material transfer, packaging, assembly, and electrical wiring. To achieve precise linear motions, most of these high-performance manufacturing machines use X - Y sliding tables with permanent-magnet rotary motors and rotary to linear couplers. Though this method is the most widely used, it has disadvantages of low accuracy, complex mechanical adjustments, high cost, and low reliability.

This paper describes the position control of a linear switched reluctance motor for high-performance motions in manufacturing automation. The proposed actuator has a very simple structure and it can be manufactured easily. There is no need for magnets and no limitation on the travel distance. The actuator is extremely robust and can be used in a hostile environment. A novel current-force-position lookup table is first developed to perform the force linearization. Then, a plug-in robust compensator using \mathcal{H}_∞ loop-shaping design is employed to improve the system robustness and the tracking performance. Experimental results of the motion system indicate that the system has fast tracking responses with good accuracy.

Index Terms—Linear switched reluctance motor (LSRM), lookup table force linearization, plug-in robust compensator, \mathcal{H}_∞ loop-shaping design, position control, precision manufacturing automation.

I. INTRODUCTION

LINEAR switched reluctance motors (LSRMs) have never been popular choices for high-precision and high-speed motion actuators because the control of LSRMs is difficult and high force ripples are always present at the output. In addition, the characteristics of an LSRM is highly dependent on its complex magnetic circuit which is difficult to model, simulate and control. There is little focus in the recent literature concerning the high-performance motion control of switched reluctance linear drive systems. It is only in recent years that we have seen a general surge of interest in the SRM [1]–[4]. This is mostly due to the advancement of power electronics, digital

signal processing, and the advanced control algorithms for non-linear systems.

The present literature on LSRM development seldom targets high-precision position control applications such as semiconductor bonding machines and pick-and-place machines. In [5] and [6], the development of an LSRM is discussed but the application of this LSRM is mainly for transportation systems, and the control output is velocity. In [7] and [8], a detailed motor design procedure and the motor control algorithm are given but its control output is again velocity. In [9] and [10], the development of two LSRMs using the double-sided configuration is addressed; however, this motor configuration is not suitable for applications that have mechanical moving parts installed on one of the motor surfaces.

The purpose of this project is to develop a high-performance direct-drive linear motion actuator system for precision position control applications. The actuator is based on the switched reluctance technology [1], [4]. The linear direct-drive actuator has a simple and robust structure, and is particularly suitable for high-precision and high-speed manufacturing machines. Manufacturing of the actuator is simple, and it is suitable for precision travel over long distances. In addition, mechanical couplings, lead screws, magnets and brushes, and special mechanical adjustments or alignments are not required in a switched reluctance linear actuator [4]. Compared to a PM linear motor, the proposed actuator has a much simpler structure and is less expensive. It is also more robust and more fault tolerant, and has less overheating problems.

Precision position motions are commonly found in industrial applications such as material transfer, packaging, assembly, and electrical wiring. The motion controller design may be different for long- and short-distance position profiles so as to compensate for the nonlinearity and model deviation; hence, the complexity of the controller implementation is increased. In this paper, position control of an LSRM is discussed. A plug-in robust compensator is proposed to improve the system robustness and the position profile tracking responses.

The organization of this paper is as follows. The design of the LSRM and its modeling are reviewed in Section II. In Section III, the feedback linearization current controller, the lookup table force linearization scheme, and the plug-in robust compensator using \mathcal{H}_∞ loop shaping design are discussed. In Section IV experimental results are presented to validate the proposed controller. Concluding remarks are given in Section V.

II. DESIGN AND MODELING OF THE LSRM

The proposed LSRM can become a direct replacement for PM linear motors. The magnet-free feature of the LSRM makes it

Paper IPCSD 03-072, presented at the 2001 Industry Applications Society Annual Meeting, Chicago, IL, September 30–October 5, and approved for publication in the IEEE TRANSACTIONS ON INDUSTRY APPLICATIONS by the Industrial Drives Committee of the IEEE Industry Applications Society. Manuscript submitted for review December 1, 2001 and released for publication June 3, 2003. This work was supported by the Research Grants Council under Competitive Earmarked Research Grant PolyU5100/99E.

W.-C. Gan was with the Department of Electrical Engineering, The Hong Kong Polytechnic University, Kowloon, Hong Kong. He is now with ASM Assembly Automation HK Ltd., Hong Kong.

N. C. Cheung is with the Department of Electrical Engineering, The Hong Kong Polytechnic University, Kowloon, Hong Kong (e-mail: eencheun@polyu.edu.hk).

L. Qiu is with the Department of Electrical and Electronic Engineering, The Hong Kong University of Science and Technology, Kowloon, Hong Kong.

Digital Object Identifier 10.1109/TIA.2003.816502

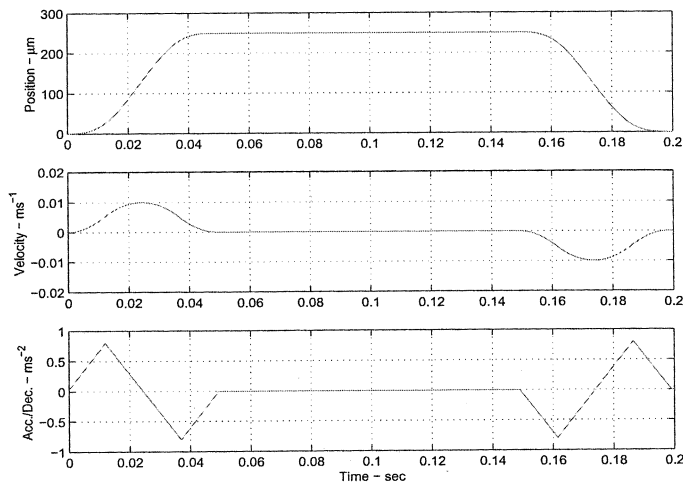


Fig. 1. Short-distance position S-profile.

particularly suitable for long- and short-distance travel in comparison to PM linear motors. In a PM linear drive system, the installation of the PMs along a long track is not an easy task. In addition, the strong magnetic attraction force of PMs creates another problem during the practical machine operation. However, all the above problems can be solved using the proposed LSRM. In this section, the design and the modeling of the LSRM are reviewed.

A. Profile Tracking Specifications

Every mechanical system has a limited control bandwidth; hence, a step input cannot be tracked accurately because of its infinite bandwidth. In order to avoid an undesired output response, a third-order position S-profile with a limited input bandwidth is used in the proposed LSRM system so that the output position can track the reference command accurately. Equation (1) governs the third-order S-profile generation

$$\begin{aligned} \frac{da(t)}{dt} &= \{J_{\max}, 0, -J_{\max}\} \\ v(t) &= \int a(t)dt \\ s(t) &= \int v(t)dt \end{aligned} \quad (1)$$

where $a(t)$, $v(t)$, and $s(t)$ are the acceleration, velocity, and position of the S-profile, respectively, while J_{\max} is a preset jerk constant. For our LSRM, two typical position profiles derived from a pick-and-place automation machine need to be tracked. The frequently tracked short-distance position profile (250 μm) is shown in Fig. 1. Another long-distance position profile that the LSRM needs to be tracked is depicted in Fig. 2. This long-distance position profile has a maximum acceleration and deceleration of $A_{\max} = 2.5 \text{ g}$, a maximum velocity of $V_{\max} = 1 \text{ ms}^{-1}$ and the travel distance is 100 mm. The steady state-error of the above two position profiles should fall into $\pm 20 \mu\text{m}$. Table I summarizes the design specifications of the LSRM.

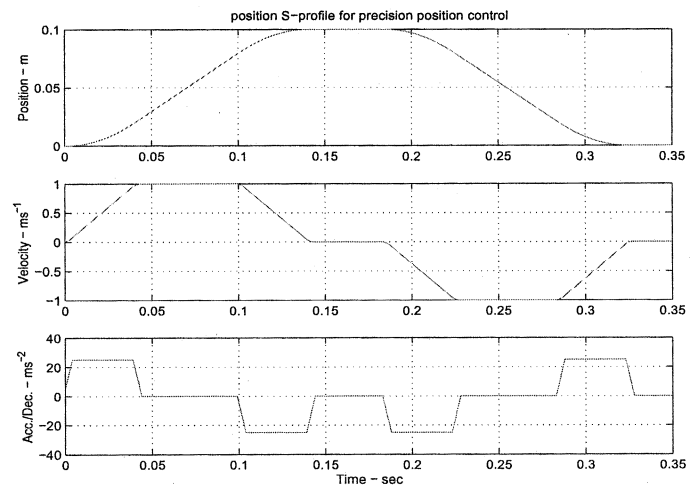


Fig. 2. Long-distance position S-profile.

TABLE I
DESIGN SPECIFICATIONS

Max loading	4.6kg
Max acceleration/deceleration	2.5g
Max velocity	1ms ⁻¹
Max travel distance	300mm
Position accuracy	$\pm 20 \mu\text{m}$

B. Configuration of the LSRM

With the specifications listed in the previous section, the mechanical dimensions of the LSRM can be derived. The first step in a LSRM design is to choose a basic magnetic path configuration and a motor winding scheme [11]. For the proposed LSRM, a single sided and longitudinal magnetic path configuration is chosen. Three-phase flux-decoupled motor windings are employed in the proposed LSRM. The reasons for our choices are as follows.

- For linear motors required to install moving mechanical parts on one of the motor surfaces, the use of a single-sided configuration is more suitable than that of a double-sided configuration.
- Zero mutual inductances between the motor windings can be achieved using the three phase flux-decoupled motor windings [5], [20].
- The individual phase motor winding reduces the manufacturing cost and complexity.
- A long travel distance can be accomplished easily by combining the longitudinal stator tracks.
- In comparison to the fixed motor windings mounted on the bottom track, the moving coil windings cause smaller average winding inductances; therefore, a low dc supply voltage ($\leq 150 \text{ V}$) power converter can still be used, and a high current loop bandwidth can be achieved. Eventually, the electromagnetic interference (EMI) problem can be reduced in a practical environment due to the low supply voltage.

Fig. 3 shows the design schematic of the LSRM. A high-grade linear motion guide from IKO Nippon Thompson Company Ltd. is chosen, so that a smooth sliding motion of the motor moving

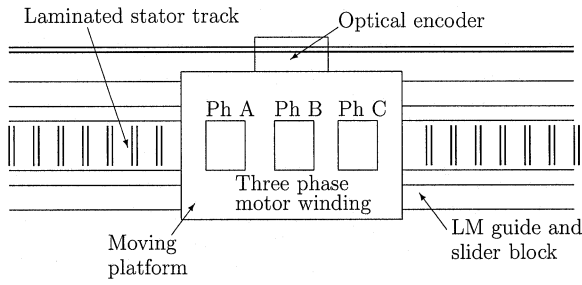


Fig. 3. Schematic of the LSRM.

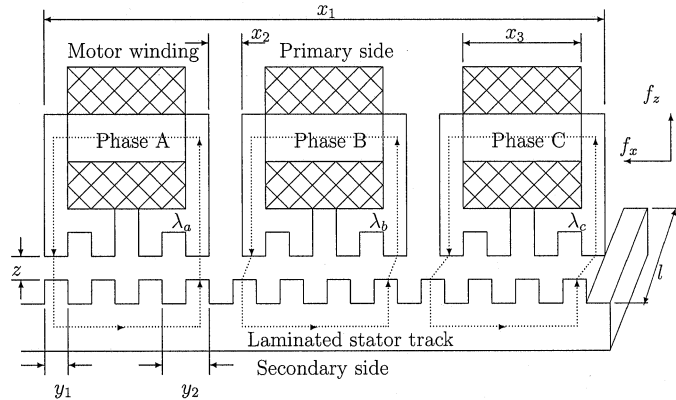


Fig. 4. Three-phase flux-decoupled motor windings.

platform can be ensured. The body and the moving platform of the LSRM are manufactured using lightweight aluminum, so that the total weight of the LSRM and the inertia of the moving platform are low. The track guide and the core of the windings are laminated with 0.5-mm silicon-steel plates. All the laminated plates are produced using a standard press tool. A 0.5- μ m resolution linear optical encoder from Renishaw Inc. is mounted on the motion actuator to observe the motion profile and provides the feedback position. In a high precision linear motion system, the expensive linear motion guide and linear optical encoder are the basic elements that cannot be excluded; however, the total cost can still be reduced greatly with the proposed low-cost laminated motor winding core and the bottom track when compared to the expensive PMs in a linear PM drive system. The three-phase coil arrangement is shown in Fig. 4. The mechanical dimensions listed in the diagram need to be designed. The three phase windings are separated with 120 electrical degrees. The flux-decoupled paths $\lambda_a(t)$, $\lambda_b(t)$, and $\lambda_c(t)$, are depicted in Fig. 4. The 3×3 flux coupling matrix can be simplified to a diagonal one with the zero mutual inductances [5]. The nonlinear mathematical model of the LSRM can be described by the following equations:

motor winding voltage balancing equations

$$v_j(t) = R_j i_j(t) + 1 \frac{\partial \lambda_j(i_j(t), x(t))}{\partial x(t)} \frac{dx(t)}{dt} + \frac{\partial \lambda_j(i_j(t), x(t))}{\partial i_j(t)} \frac{di_j(t)}{dt} \quad (2)$$

$j = a, b, c$

TABLE II
MOTOR MECHANICAL AND ELECTRICAL PARAMETERS

Pole width (y_1)	5mm
Pole pitch (y_2)	10mm
Motor length (x_1)	121.666mm
Phase separation (x_2)	8.333mm
Winding length (x_3)	15mm
Winding width (l)	25mm
Air gap width (z)	0.5mm
Number of turns per phase (N)	159
Rated power	115W
Aligned inductance	19.2mH
Unaligned inductance	11.5mH
Phase resistance	1.6 Ω
Peak force generation per phase	115N

torque equations

$$f_x(i_a(t), i_b(t), i_c(t), x(t)) = \sum_{j=a}^c f_j(i_j(t), x(t)) = \sum_{j=a}^c \frac{\partial \int_0^{i_j(t)} \lambda_j(i_j(t), x(t)) di_j(t)}{\partial x(t)} \quad (3)$$

$$f_x(i_a(t), i_b(t), i_c(t), x(t)) = M_m \frac{d^2 x(t)}{dt^2} + B_m \frac{dx(t)}{dt} + f_l(t) \quad (4)$$

where $v_j(t)$, $i_j(t)$, and R_j are the phase voltage, phase current, and phase resistance, respectively, $\lambda_j(i_j(t), x(t))$ and $f_j(i_j(t), x(t))$ are the phase flux linkage and phase electromechanical force of the x axis, $x(t)$ is the travel distance, $f_x(i_a(t), i_b(t), i_c(t), x(t))$ is the total generated electromechanical force of x axis, $f_l(t)$ is the external load force, and M_m and B_m are the mass and the friction constant, respectively.

C. Review of the LSRM Design

According to the specifications listed in Table I, the mechanical dimensions shown in Fig. 4 can be figured out. The design procedure and the experimental verification can be found in [20]. The mechanical and electrical parameters of the LSRM are summarized in Table II and the LSRM model is shown in Fig. 5.

D. Modeling of the LSRM

The nonlinear model of the proposed LSRM is discussed in this section. The nonlinear model of the LSRM is given by

$$f_x(i_a(t), i_b(t), i_c(t), x(t)) = \sum_{j=a}^c f_j(i_j(t), x(t)) = M_m \frac{d^2 x(t)}{dt^2} + B_m \frac{dx(t)}{dt} + f_l(t).$$

This mathematical model consists of two parts. The first part is the linear model for the mechanical linkage while the second part is the nonlinear force generation function. The mechanical parameters M_m and B_m can be easily found using standard experiments. The total nonlinear force generation

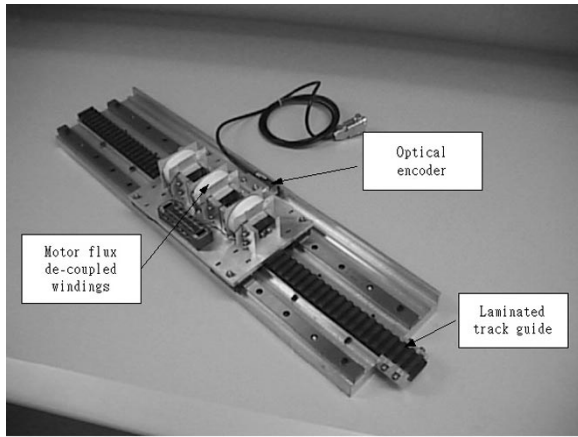


Fig. 5. LSRM model.

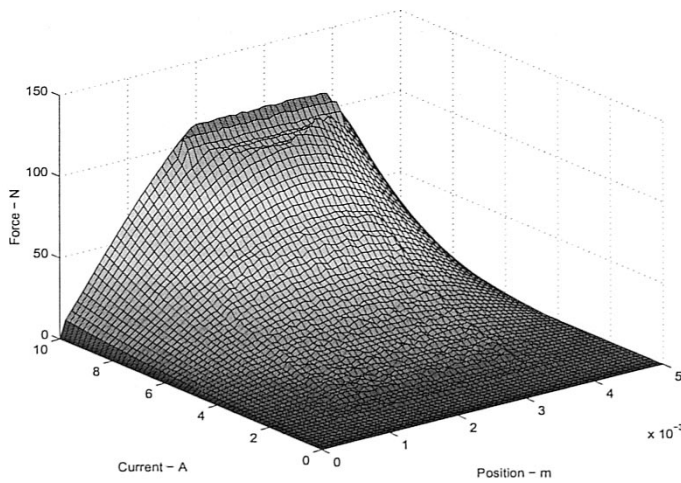
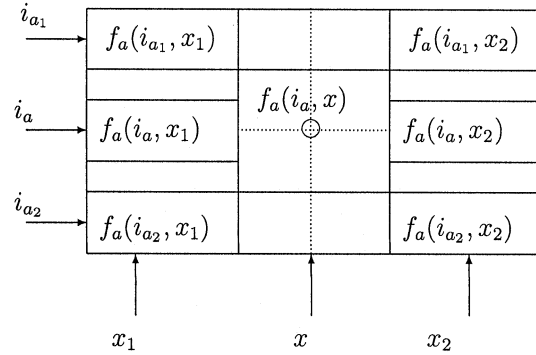


Fig. 6. Experimental force-current-position 3-D chart.

function $f_x(i_a(t), i_b(t), i_c(t), x(t))$ has three components $f_a(i_a(t), x(t))$, $f_b(i_b(t), x(t))$ and $f_c(i_c(t), x(t))$; however, as these three functions are identical, the modeling of the total force generation function can be derived from the modeling of the force generation function for one phase $f_j(i_j(t), x(t))$. Therefore, a three-dimensional (3-D) force-current-position graph of the phase-*A* winding is measured experimentally to capture both the linear and saturation regions of the proposed LSRM.

A mechanical test rig is employed to measure the force-current-position 3-D chart. This test rig can accurately divide the 5-mm pole width into 60 divisions using high-precision screws and gears. In the experiment, the test rig is used to lock the moving platform at 61 discrete positions (60 divisions) within a pole width (5 mm), and then 61 discrete phase current values (from 0 to 10 A) are injected into the motor coil. Next, the generated force value can be read from the load cell installed in the mechanical test rig. The choice of the 61 discrete positions is to ensure that an accurate measurement can be done using the mechanical test rig. A special mechanical test rig may need to be redesigned if other than the choice of the 61 discrete positions are opted for. The experimental force-current-position 3-D chart is shown in Fig. 6.

Fig. 7. Calculating f_a from the lookup table.

The data outside the grid can be obtained using a simple but effective two-dimensional linear interpolation scheme and a lookup table. This method was applied successfully in the modeling and control of a highly nonlinear solenoid [12], [13]. Fig. 7 shows the method of obtaining the phase-*A* electromechanical force $f_a(i_a(t), x(t))$ by the two-dimensional linear interpolation scheme. When the inputs $i_a(t)$ and $x(t)$ enter the lookup table, the following four data points can be located as:

$$f_a(i_{a1}, x_1), f_a(i_{a2}, x_1), f_a(i_{a1}, x_2), f_a(i_{a2}, x_2)$$

where $i_{a1} \leq i_a(t) \leq i_{a2}$ and $x_1 \leq x(t) \leq x_2$. Then, the two intermediate values can be obtained using the following equations:

$$f_a(i_a(t), x_1) = f_a(i_a(t), x_1) + \left(\frac{i_a(t) - i_{a1}}{i_{a2} - i_{a1}} \right) \times [f_a(i_{a2}, x_1) - f_a(i_{a1}, x_1)]$$

$$f_a(i_a(t), x_2) = f_a(i_a(t), x_2) + \left(\frac{i_a(t) - i_{a1}}{i_{a2} - i_{a1}} \right) \times [f_a(i_{a2}, x_2) - f_a(i_{a1}, x_2)].$$

Finally, the output force value is given by

$$f_a(i_a(t), x(t)) = f_a(i_a(t), x_1) + \left(\frac{x(t) - x_1}{x_2 - x_1} \right) \times [f_a(i_a, x_2) - f_a(i_a, x_1)].$$

An LSRM model using the $61 \times 61 = 3721$ data grid is developed in the MATLAB/SIMULINK environment. This motor model is used in the simulations of the motor controller design and evaluation.

The second experiment is done to find out the relationship of the current-force-position needed for the force linearization scheme in the real-time controller implementation. The experiment is conducted by fixing the moving platform at 61 discrete positions within a pole width (5 mm). Then the current required to generate the force at 61 discrete values from 0 to 110 N is measured. The experimental data are shown in Fig. 8.

The current-force-position lookup table is the main component of the real-time controller, and is used to perform the force linearization which will be introduced in the next section. However, the data size (3721 data points) may be too large for embedded low-cost microcontrollers/digital signal processors (DSPs). We limit the table size within 512 data points so that the developed force linearization scheme can be implemented using low-cost microcontrollers/DSPs with small memory spaces. As

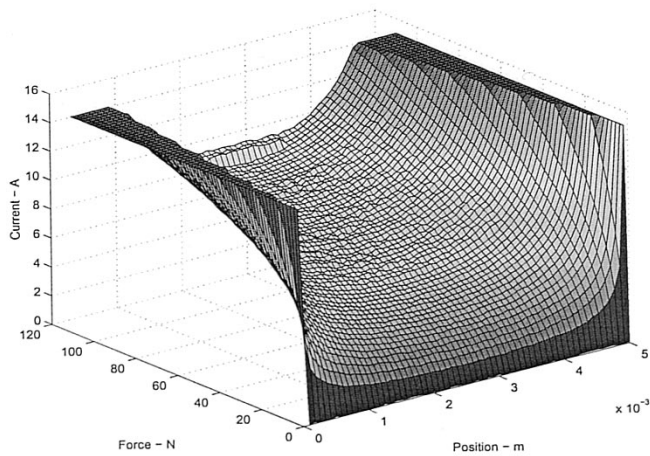


Fig. 8. Experimental current–force–position 3-D chart.

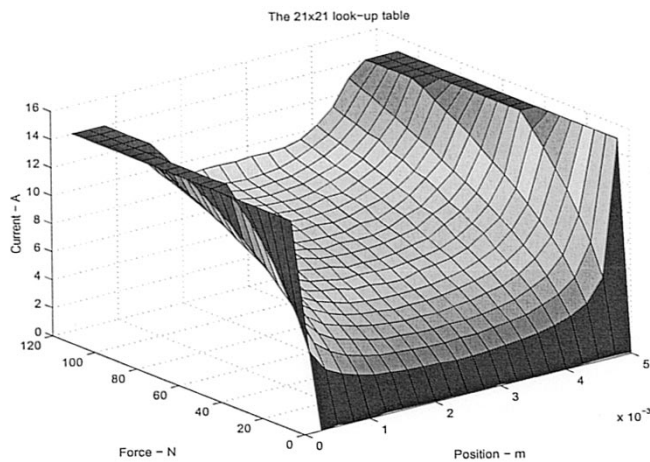


Fig. 9. 21 × 21 current–force–position 3-D chart.

stored in the real-time controller is a sampled version of Fig. 8, a table size of $21 \times 21 = 441$ is selected to fulfill the 512 data point requirement. Therefore, a 3-D lookup table using the $21 \times 21 = 441$ data that are sampled from the original mesh is developed for the real-time implementation of the motor controller. The 21×21 current–force–position 3-D chart is shown in Fig. 9. The required current $i_j(f_j(t), x(t))$ is again found using the two-dimensional linear interpolation scheme and the lookup table that we introduced before.

To qualify the small but effective current–force–position lookup table, an error-budget analysis is performed. Fig. 10 shows the absolute error plot between the data interpolated by the proposed scheme and the actual experimental data. It is found that the maximum error is around 1 A, 10% of the maximum nominal current of the motor driver. The maximum error is located at the turning corners of the saturation region because a linear interpolation scheme is not capable of mimicking sharp turning corners. Except for the two small regions, the small lookup table can interpolate accurate data for other areas. This justifies the tradeoff between the size of the lookup table and the interpolation accuracy.

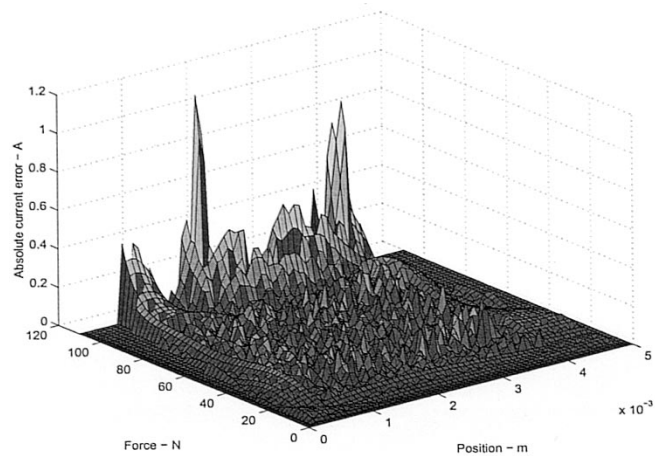


Fig. 10. Error analysis.

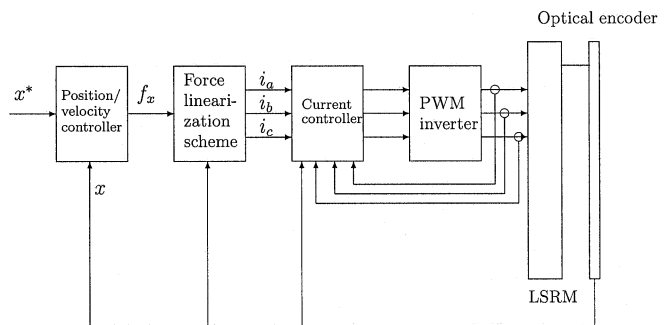


Fig. 11. Overall control block diagram for the LSRM.

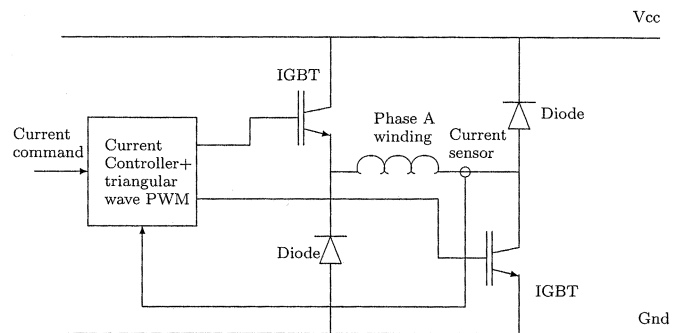


Fig. 12. Asymmetric bridge PWM inverter.

III. CONTROLLER DESIGN FOR THE LSRM

Exploiting the fact that the current dynamics is at least an order faster than the mechanical dynamics, a dual-rate cascade control approach is proposed. A fast inner loop current controller is employed to track the currents present at the motor terminals, while a slower outer loop trajectory controller is used to track the reference position profiles. A current–force–position lookup table, introduced in the previous section, is employed to perform the force linearization. Fig. 11 shows the overall block diagram of the control system.

Three asymmetric bridge pulsewidth-modulation (PWM) inverters are used in the current tracking amplifier. Fig. 12 shows the inverter setup for one phase. The asymmetric inverter configuration is employed to drive the LSRM, so that high

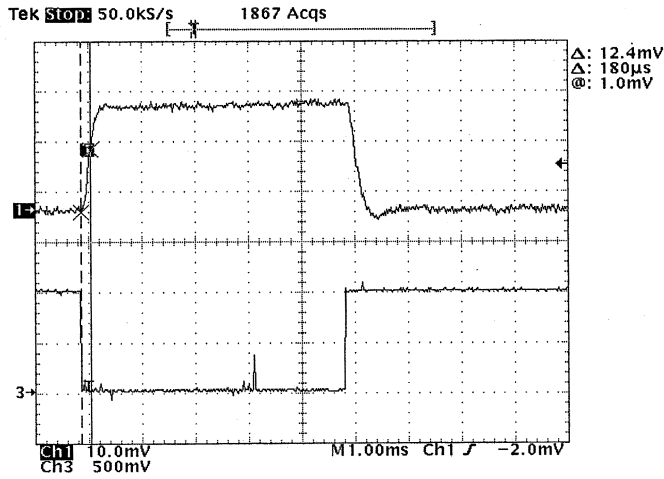


Fig. 13. Current step response at the aligned position (output current 10 mV = 1 A).

dynamic responses can be enjoyed independently in each motor phase [1].

As the LSRM is a unipolar current driving actuator, only two insulated gate bipolar transistors (IGBTs) are needed in a single-phase asymmetric inverter and the two diodes are used for the current return path. With the help of the PWM modulator, the relationship between the output current and the input voltage for one phase motor winding is represented by the following differential equation [7]:

$$\frac{di_j(t)}{dt} = -\frac{R_j}{L_j(x(t))}i_j(t) + \frac{K_j}{L_j(x(t))}u_j(t) \quad (5)$$

where K_j is the converter gain, $L_j(x(t))$ is the phase inductance which varies with position, R_j is the phase resistance, $u_j(t)$ is the control input, and $i_j(t)$ is the control output. The proposed control law, which is a proportional-derivative (PD) controller with the feedback linearization, is as follows:

$$u_j(t) = \frac{L_j(x(t))}{K_j} \left[\frac{R_j}{L_j(x(t))}i_j(t) + \frac{di_j^*(t)}{dt} + K_p(i_j^*(t) - i_j(t)) \right] \quad (6)$$

where $i_j^*(t)$ is the command reference, K_p is a positive constant, and $L_j(x(t))$ is the inductance value that is measured experimentally. Substituting (6) into (5), the closed-loop system is governed by

$$\left(\frac{di_j^*(t)}{dt} - \frac{di_j(t)}{dt} \right) + K_p(i_j^*(t) - i_j(t)) = 0. \quad (7)$$

With a proper choice of K_p , the current error $(i_j^*(t) - i_j(t)) \rightarrow 0$ as $t \rightarrow \infty$. Therefore, the output $i_j(t)$ converges to the reference input $i_j^*(t)$ asymptotically.

The current controller is implemented using the above proposed control law and the experimental results are shown in Figs. 13 and 14, respectively. As the error (7) is a first-order differential equation, an overshoot-free step response can be enjoyed automatically. In addition, $K_p = 6500$ is chosen for this example so as to achieve an approximately 1-kHz current loop bandwidth. The 1-kHz current loop bandwidth is adequate for many applications because the outer position loop bandwidth is around 100 Hz, generally. Fig. 13 shows the current

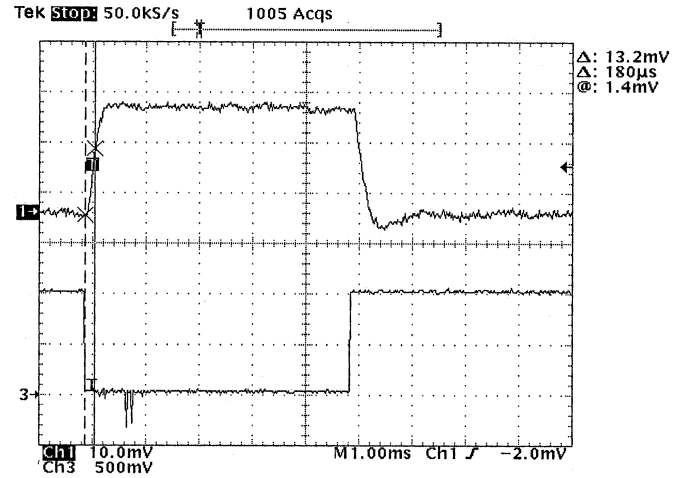


Fig. 14. Current step response at the unaligned position (output current 10 mV = 1 A).

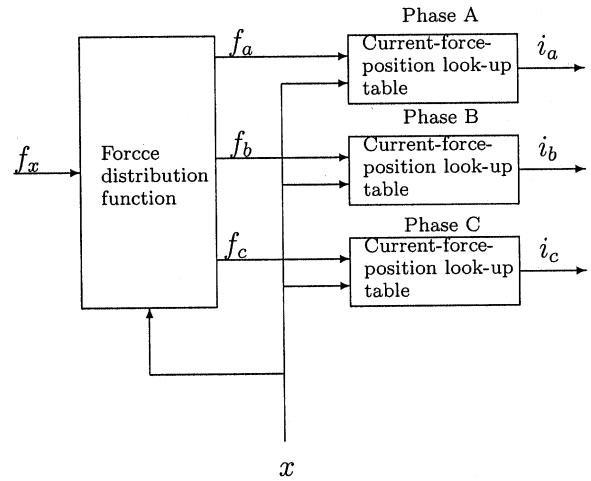


Fig. 15. Two-stage force linearization scheme.

step response when the motor winding is at the aligned position at which the phase inductance attains its maximum value. The output does not exhibit any overshoot when the proposed current controller is used. The rise time, approximately equal to $180 \mu\text{s}$, is equivalent to a 1.2-kHz bandwidth.

Next, the current response is measured in Fig. 14 when the motor winding is at the unaligned position at which the phase inductance attains its minimum value. As the inductance variation is compensated by the proposed controller, the overshoot-free step response and the $180\text{-}\mu\text{s}$ rise time are still maintained. The proposed controller used in the current loop can ensure a desirable tracking response, so the perfect current tracking condition can be assumed in the outer loops with slow dynamics.

The nonlinear motor controller includes the force linearization scheme which consists of two stages. In the first stage, the force command is resolved into three components, $f_a(t)$, $f_b(t)$, and $f_c(t)$. For each phase, the current-force-position lookup table introduced in the previous section is employed to calculate the three-phase desired currents $i_a(t)$, $i_b(t)$, and $i_c(t)$. Fig. 15 shows the block diagram of the two-stage force linearization scheme.

TABLE III
PHASE EXCITATION TABLE FOR A SINGLE-POLE PITCH (0 mm = THE FULLY
ALIGNED POSITION OF PHASE WINDING A)

Region	Position range (mm)	+ve force command	-ve force command
1	0-1.6666	B	C,A
2	1.6666-3.3333	B,C	A
3	3.3333-5	C	A,B
4	5-6.6666	C,A	B
5	6.6666-8.3333	A	B,C
6	8.3333-10	B,A	C

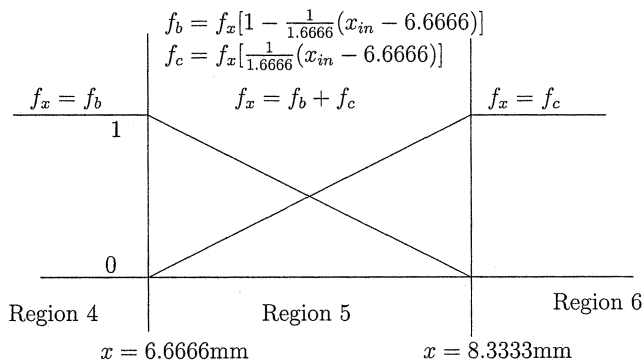


Fig. 16. Force distribution example in region 5 for a negative force command.

Table III shows the phase excitation table of the proposed linear actuator for a single pole pitch (10 mm). For example, if the current position falls in region 5 and the required force command is a negative value, then phase-B and/or phase-C windings can be energized so as to produce the required force command. On the other hand, if the force command is a positive value, then only phase A can be energized to generate the command force in region 5. A linear function is proposed to perform the force distribution when a two-phase excitation is needed. Fig. 16 shows a force distribution example when the current position falls in region 5 and the force command is a negative value.

Tables IV and V show the detailed force distribution functions for both positive and negative force commands. The proposed linear force distribution function can improve the force transition between phase switching without any implementation of complex mathematical functions.

The current-force-position lookup table is then used in the second stage to perform the nonlinearity compensation. The small lookup table (21×21 elements, with increments of 0.5 A and 5.5 N) described in the previous section is employed to perform the force linearization. The two-dimensional linear interpolation is again used to find the reference current values. Fig. 17 shows how the required phase-A current $i_a(f_a(t), x(t))$ can be evaluated using the two-dimensional linear interpolation scheme discussed in Section II.

With the proposed lookup table force linearization scheme, a simple yet effective nonlinear controller is developed for the linear switched reluctance actuator without the implementation of complex mathematical functions such as sine, cosine, and square root functions. Hence, it is particularly suitable for a low-cost implementation.

The trajectory controller forms the essential part of the slow subsystem. A two-degrees-of-freedom (2DOF) controller

shown in Fig. 18 is used in the proposed LSRM drive system. With the current-tracking controller and the proposed force linearization scheme, the nominal system plant can be represented by a linear system as

$$P(s) = \frac{1}{s(M_m s + B_m)}. \quad (8)$$

The simplest choice for the 2DOF controller is the PD compensator,

$$K(s) = C(s) = [C_1(s) - C_2(s)] = \frac{1}{\delta_1 s + 1} \times [K_{d1}s + K_{p1} - (K_{d2}s + K_{p2})]$$

where δ_1 is a small positive constant. The low-pass filter $1/(\delta_1 s + 1)$ is used for the differentiation noise filtering. With the 2DOF controller, the closed-loop transfer function is given by

$$\frac{X(s)}{X^*(s)} \approx \frac{K_{d1}s + K_{p1}}{M_m s^2 + (B_m + K_{d2})s + K_{p2}}.$$

The desired closed-loop poles can be achieved by choosing the gains K_{p2} and K_{d2} properly while the desired closed-loop zero can be assigned by placing suitable values in K_{p1} and K_{d1} . In order to compensate for the nonlinearity and the system plant uncertainty, a plug-in robust compensator is proposed to add on top of the controller structure in Fig. 11 so as to enhance the system robustness.

A. Design of the Plug-in Robust Compensator

When there are system perturbations such as system plant parameter variations, chattering effects caused by the lookup table force linearization, and the change of operating points (from long-distance position profile to short-distance position profile tracking), model uncertainty happens and, hence, the nominal plant in (8) cannot represent the real system completely. This also explains why the motion controller parameters are always different for different distance position profile tracking. In this section a plug-in robust compensator is proposed to compensate for the model uncertainty in the presence of the system perturbations, so that only one set motion controller parameter with the plug-in compensator can be used for tracking all-distance position profiles. The novel feature of the proposed plug-in robust compensator is that the reference tracking and system robustness specifications can be designed separately. A desirable reference tracking transfer function can be designed using a simple nominal controller $C(s)$, and then the system robustness can be taken care using the plug-in compensator [19].

The general feedback system with a 2DOF controller is shown in Fig. 18. Assume $P(s)$ is a single-input-single-output (SISO) strictly proper nominal system. In our LSRM system, the nominal plant is equal to $P(s) = 1/(s(M_m s + B_m))$. Initially, assume that the 2DOF controller $K(s) = [K_1(s) - K_2(s)]$ is given by $K(s) = C(s) = [C_1(s) - C_2(s)]$ which is the existing controller employed in the previous section.

Let a coprime factorization of $P(s)$ be given as

$$P(s) = \frac{N(s)}{M(s)}$$

TABLE IV
FORCE DISTRIBUTION TABLE FOR +ve FORCE COMMANDS f_x (x IN MILLIMETERS)

Region	f_a	f_b	f_c
1	0	f_x	0
2	0	$f_x \left[1 - \frac{1}{1.6666}(x - 1.6666) \right]$	$f_x \left[\frac{1}{1.6666}(x - 1.6666) \right]$
3	0	0	f_x
4	$f_x \left[\frac{1}{1.6666}(x - 5) \right]$	0	$f_x \left[1 - \frac{1}{1.6666}(x - 5) \right]$
5	f_x	0	0
6	$f_x \left[1 - \frac{1}{1.6666}(x - 8.3333) \right]$	$f_x \left[\frac{1}{1.6666}(x - 8.3333) \right]$	0

TABLE V
FORCE DISTRIBUTION TABLE FOR -ve FORCE COMMANDS f_x (x IN MILLIMETERS)

Region	f_a	f_b	f_c
1	$f_x \left[\frac{1}{1.6666}x \right]$	0	$f_x \left[1 - \frac{1}{1.6666}x \right]$
2	f_x	0	0
3	$f_x \left[1 - \frac{1}{1.6666}(x - 3.3333) \right]$	$f_x \left[\frac{1}{1.6666}(x - 3.3333) \right]$	0
4	0	f_x	0
5	0	$f_x \left[1 - \frac{1}{1.6666}(x - 6.6666) \right]$	$f_x \left[\frac{1}{1.6666}(x - 6.6666) \right]$
6	0	0	f_x

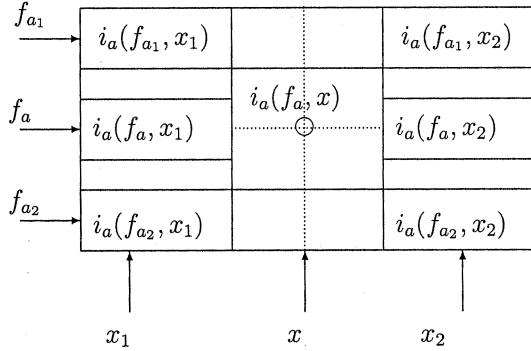


Fig. 17. Calculating i_a from the lookup table.

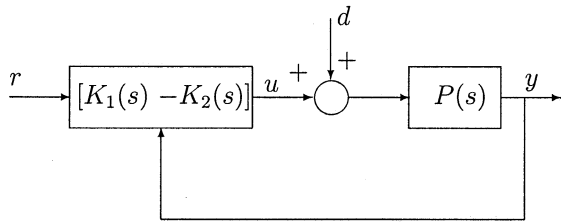


Fig. 18. General 2DOF controller.

where $M(s), N(s) \in \mathcal{H}_\infty$. Since $C(s)$ is a stabilizing 2DOF controller for $P(s)$, for any coprime factorization

$$C(s) = \frac{[X_1(s) - X_2(s)]}{Y_0(s)}$$

where $X_1(s), X_2(s)$, and $Y_0(s) \in \mathcal{H}_\infty$. It is shown in [17, Th. 15 of Sec. 5.6] that all 2DOF stabilizing controllers can be parameterized as

$$[K_1(s) - K_2(s)] = \frac{[S(s) - (X_2(s) + Q(s)M(s))]}{(Y_0(s) - Q(s)N(s))} \quad (9)$$

where $Q(s) \in \mathcal{H}_\infty$ and $S(s) \in \mathcal{H}_\infty$ are arbitrary stable systems. If we plug $K(s) = [K_1(s) - K_2(s)]$ to the feedback system, then the transfer function from $r(t)$ to $y(t)$ becomes

$$\frac{Y(s)}{R(s)} = \frac{N(s)S(s)}{Y_0(s)M(s) - X_2(s)N(s)}$$

which is independent of $Q(s)$. Assume that the system plant controlled using the nominal controller $C(s)$ can achieve a satisfactory transfer function from $r(t)$ to $y(t)$. We would like to keep this transfer function after adding the plug-in compensator, it then follows that we can choose $S(s) = X_1(s)$ since

$$\begin{aligned} \frac{Y(s)}{R(s)} &= \frac{N(s)S(s)}{Y_0(s)M(s) - X_2(s)N(s)} \\ &= \frac{C_1(s)P(s)}{1 + C_2(s)P(s)} \\ &= \frac{N(s)X_1(s)}{Y_0(s)M(s) - X_2(s)N(s)}. \end{aligned}$$

Therefore, the set of all stabilizing 2DOF controllers which gives the same nominal tracking performance is given by

$$[K_1(s) - K_2(s)] = \frac{[X_1(s) - (X_2(s) + Q(s)M(s))]}{(Y_0(s) - Q(s)N(s))}.$$

The loop property of the feedback system, which depends on $K_2(s)$ and $P(s)$ only, now depends on $Q(s)$ only. For any stable system $Q(s)$, which can even be nonlinear and time varying, the nominal tracking performance is unaffected and the closed-loop stability is guaranteed [14], [18]. Suppose that a $Q(s)$ is chosen, theoretically there are two ways to implement the new controller $K(s)$. One is to explicitly obtain $K(s)$ from (9) and implement as in Fig. 18. The other way is to use the structure in Fig. 19. Clearly, the first way requires the dismantling of the original controller $C(s) = [C_1(s) - C_2(s)]$. It is the use of the structure in Fig. 19 that gives us the plug-in feature of our additional controller. Now, we give one method to design a $Q(s)$ for enhancing the robustness of the control system.

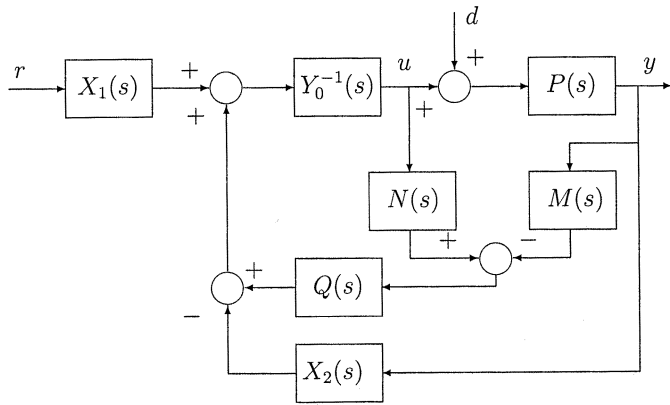


Fig. 19. Proposed plug-in robust compensator.

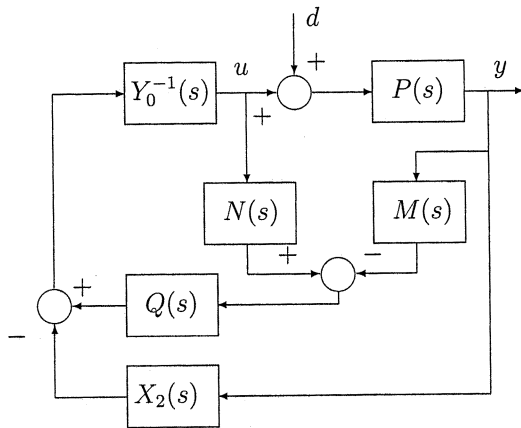
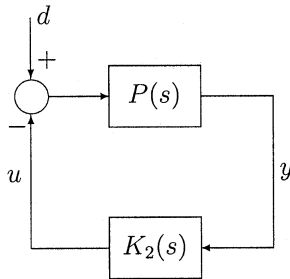
Fig. 20. Block diagram for the design of the plug-in compensator $Q(s)$.

Fig. 21. Standard feedback configuration.

B. \mathcal{H}_∞ Loop-Shaping Plug-in Compensator Design

Since the purpose of $Q(s)$ is to improve the loop property of the feedback system, the tracking issue is not of concern in its design. The feedback loop part of the whole system is redrawn in Fig. 20 with the reference injection part ignored. Fig. 20 can be simplified to Fig. 21 with $K_2(s) = X_2(s) + Q(s)M(s)/Y_0(s) - Q(s)N(s)$. Our idea in the design of a stable $Q(s)$ is to design a stabilizing $K_2(s)$ and then back substitute to get $Q(s)$ using

$$Q(s) = \frac{K_2(s)Y_0(s) - X_2(s)}{M(s) + K_2(s)N(s)} \quad (10)$$

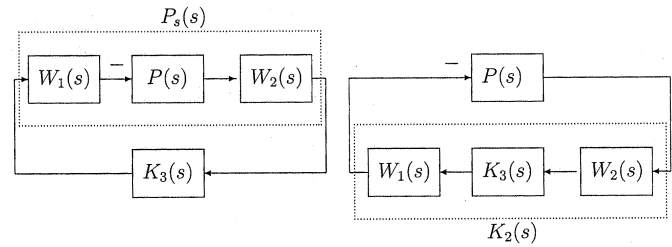
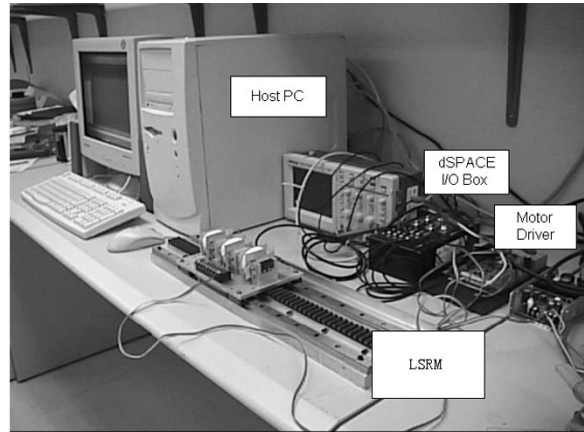
Fig. 22. An \mathcal{H}_∞ loop-shaping controller design procedure.

Fig. 23. Experimental setup in the power electronics laboratory at HKPU.

which is obtained from (9). Since all stabilizing $K_2(s)$ are obtained from

$$K_2(s) = \frac{X_2(s) + Q(s)M(s)}{Y_0(s) - Q(s)N(s)}$$

over all stable $Q(s)$, it follows that $Q(s)$ obtained from (10) for a stabilizing $K_2(s)$ has to be stable.

The design of the controller $K_2(s)$ is further divided into two steps. The first step is to choose a proper pre-filter $W_1(s)$ and post-filter $W_2(s)$ so that the shaped plant, $P_s(s) = W_1(s)P(s)W_2(s)$, has a desired open loop frequency response according to some well-defined specifications such as bandwidth or steady-state error requirement. Then, an \mathcal{H}_∞ optimal robust controller $K_3(s)$ is found to minimize

$$\left\| \begin{bmatrix} I \\ K_3(s) \end{bmatrix} (I + P_s(s)K_3(s))^{-1} \begin{bmatrix} I & P_s(s) \end{bmatrix} \right\|_\infty. \quad (11)$$

This can be done using the solution in [15] or the command *ncfsyn* of the MATLAB μ -Analysis and Synthesis Toolbox [16]. The controller $K_2(s)$ is obtained by combining the pre-filters $W_1(s)$, $W_2(s)$ and the \mathcal{H}_∞ controller $K_3(s)$ as $K_2(s) = W_1(s)K_3(s)W_2(s)$. Fig. 22 shows the \mathcal{H}_∞ loop-shaping controller design procedure. Finally, the block $Q(s)$ can be found in (10).

IV. EXPERIMENTAL RESULTS

The controller is implemented using a DSP-based system. Fig. 23 shows the actual experimental setup in the power electronics laboratory at The Hong Kong Polytechnic University (HKPU). A Pentium II computer is used for the program development and motion monitoring during the real-time execution. A DSP board, plugged into an ISA bus of the Pentium II

computer, performs all control functions. The TMS320C31 DSP has a processing rate of 33 Mflops. Four simultaneously triggered analog-to-digital converters (two 16 bits, and two 14 bits) are included into the processor board. A TMS 320P14 slave fixed-point DSP, which is tightly coupled to the TMS320C31, generates the PWM waveforms. Note that the present setup is intended for development purposes only. The proposed control scheme can be implemented using a low-cost DSP or even a microcontroller.

Three asymmetric bridge IGBT inverters are employed to drive the LSRM and a 150-V dc supply voltage is used. As the motor windings are installed on the moving side, the phase inductance average value is smaller than one with the windings installed on the bottom long track. Therefore, a low-voltage PWM inverter can still be used in the proposed LSRM system.

A crossover protection circuit is used to protect the power supply from short circuiting. Since the worst case turn off time for the IGBTs is $0.1 \mu\text{s}$, a $0.2\text{-}\mu\text{s}$ delay is introduced to the turn-on time of the IGBTs. The three-phase currents passing through the coils of the switched reluctance linear motor, are sensed by three highly sensitive Hall-effect elements. Three second-order analog active filters with cutoff frequencies of 1.5 kHz are used to filter out the high-frequency components of the current signal.

A 2-kHz sampling frequency of the position controller is chosen because the bandwidth of the position profiles is around 100 Hz, generally. To ensure that the dynamics of the current loop is much faster than that of the position loop, a sampling frequency of 8 kHz is used for the current-tracking controller. In the real-time implementation, $21 \times 21 = 441$ 16-bit memory locations are allocated for the lookup table. This small memory space is easily found and implemented in low-cost microcontrollers/DSPs. The execution times for the inner current loop control, force lookup table linearization scheme and position loop control are equal to 60, 220, and $160 \mu\text{s}$, respectively. In comparison to other force linearization schemes [6], [7], the lookup table force linearization scheme does not require implementation of any complex mathematical functions such as sine, cosine, and square root routines. Therefore, the execution time can be much reduced.

A. Experimental Results Without the Plug-in Robust Compensator

The two position profiles stated in Section II-A are used as the test inputs. The plug-in robust compensator is turned off during the experiment in this section. The first experiment is to test the tracking performance of the long-distance position profile. The full load of 4.6 kg is applied to the moving platform and the position response is shown in Fig. 24. The actual position tracks closely with the command position. The maximum dynamic error is approximately equal to $180 \mu\text{m}$ and the steady error is just below $20 \mu\text{m}$ which satisfies our design specifications. The short position profile needs to be tracked most frequently because small distance movements are indeed involved in many industrial applications such as pick-and-place movements and the semiconductor bonding processes. Fig. 25 shows the position response when the $250\text{-}\mu\text{m}$ short-distance position

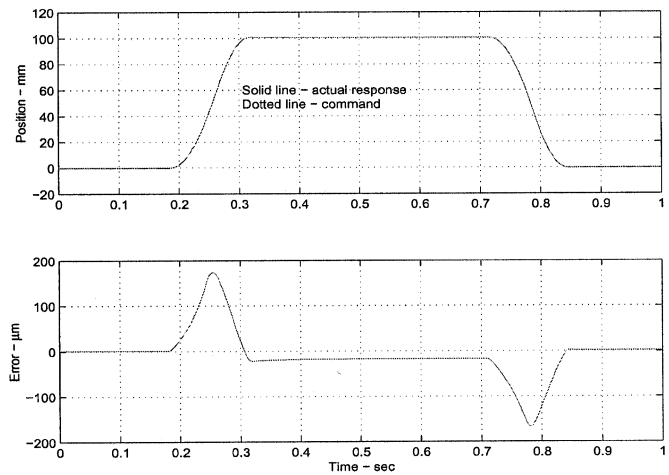


Fig. 24. Position response for the long-distance position profile.

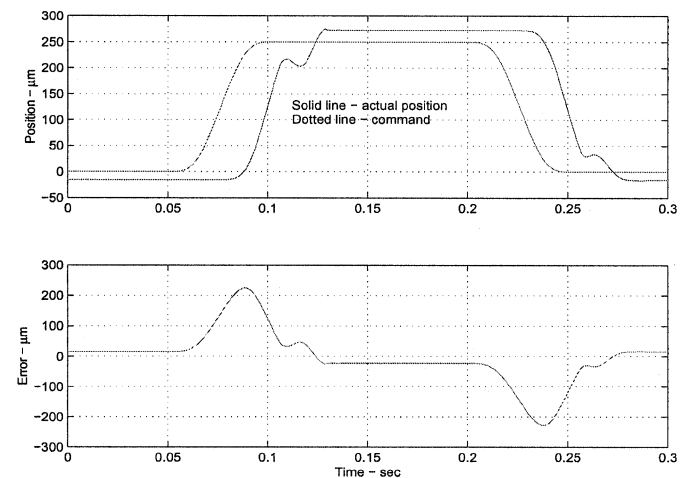


Fig. 25. Position response for the short-distance position profile.

profile is used as the test input. The output response cannot satisfy the design specifications as the steady error is larger than $20 \mu\text{m}$. In addition, overshoot and nonlinear effects are present at the output. The $210\text{-}\mu\text{m}$ dynamic error is unacceptable for a $250\text{-}\mu\text{m}$ short-distance travel.

B. Experimental Results With the Plug-in Robust Compensator

The two designed position profiles are tested again with the proposed plug-in robust compensator. Fig. 26 shows the position response when the short-distance position profile is used as the test input while Fig. 27 shows the total force command and the Phase-A output current for this profile tracking. With the help of the plug-in robust compensator, the overshoot and the nonlinear effect can be eliminated. In addition, the maximum dynamic error is reduced to $15 \mu\text{m}$ and the steady-state error is greatly improved. However, the $3.5\text{-}\mu\text{m}$ steady-state error present at the return path may be due to the nonlinear frictional force within this small distance. In addition, the peak current for this profile tracking is around 1 A and the fast-response inner current control loop (1.2-kHz bandwidth) can definitely track this command value accurately. In general, the transient tracking response of the short-distance position profile is enhanced significantly with the plug-in robust compensator.

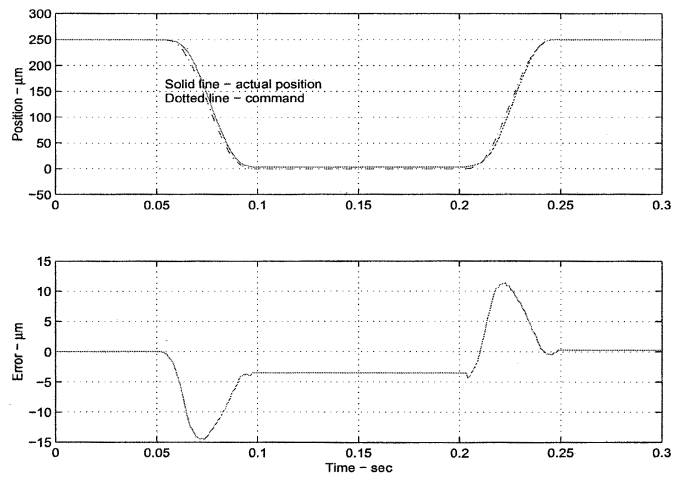


Fig. 26. Position response of the short-distance position profile with the plug-in compensator.

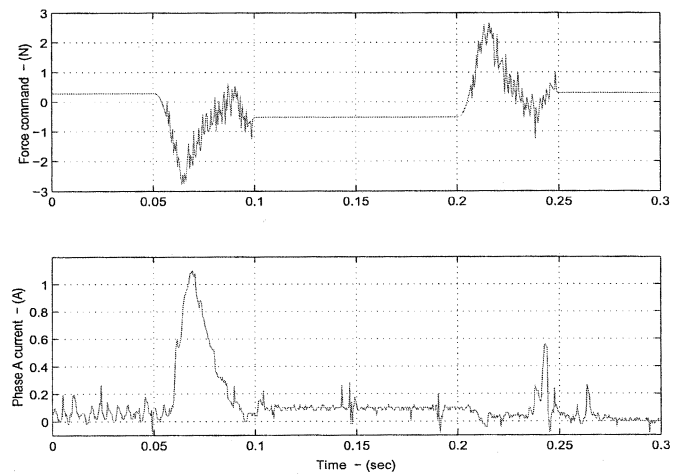


Fig. 27. Total force command and phase-A current output of the short-distance position profile.

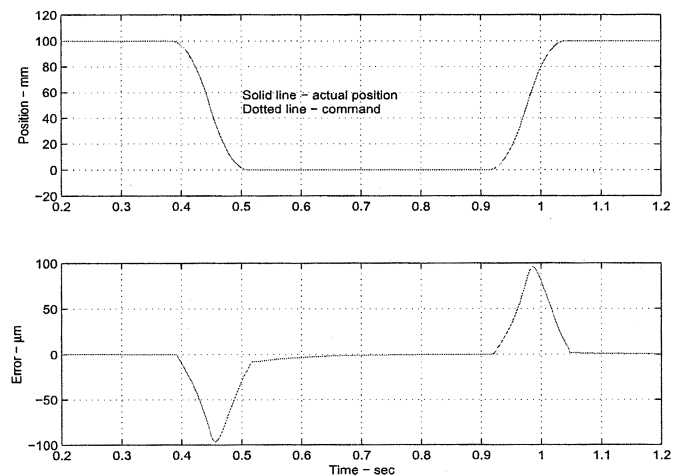


Fig. 28. Position response of the long-distance position profile with the plug-in compensator.

Fig. 28 shows the position responses of the long-distance position profile when the plug-in compensator is turned on. The

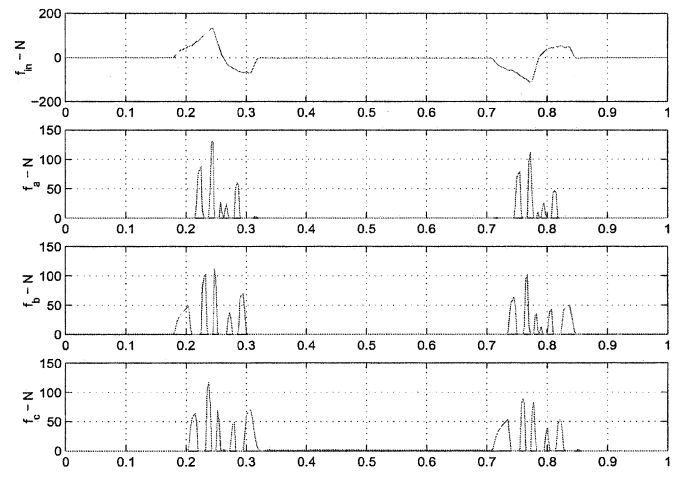


Fig. 29. Force distribution diagram.

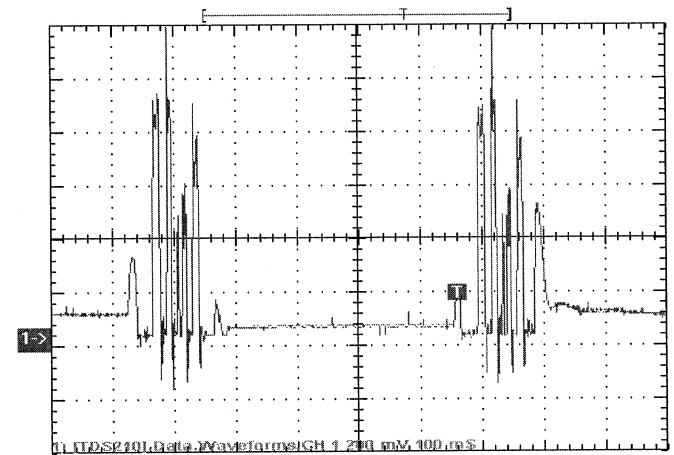


Fig. 30. Phase-A output current (100 mV = 1 A).

transient tracking response is not only without any degradation, but also has improvement in the dynamic errors and the steady-state errors. The force command and the three phase force distribution for the long-distance profile are depicted in Fig. 29. The maximum required force is about 120 N. The summation of the three-phase forces are equal to the absolute value of the command force. The phase current commands are actually scaled versions of the ones in Fig. 29. Fig. 30 shows the actual current for the phase A motor winding and this phase output current matches well with the command values. In addition, the maximum current required to achieve the peak acceleration/deceleration is approximately equal to 11 A that still falls into the motor amplifier driving capability. From the above results, the setting of 1.2-kHz inner current loop bandwidth, as described in Section III, is adequate for the current tracking requirement of this profile. In the design of the plug-in robust compensator, the crossover frequency of the overall closed-loop transfer function is set to around 100 Hz. The position error plot shown in Fig. 29 reveals that the response times of the position and force controllers are also fast enough for this profile tracking. By combining the sophisticated inner current loop controller and the outer robust plug-in compensator, the long-distance position profile can still be tracked accurately.

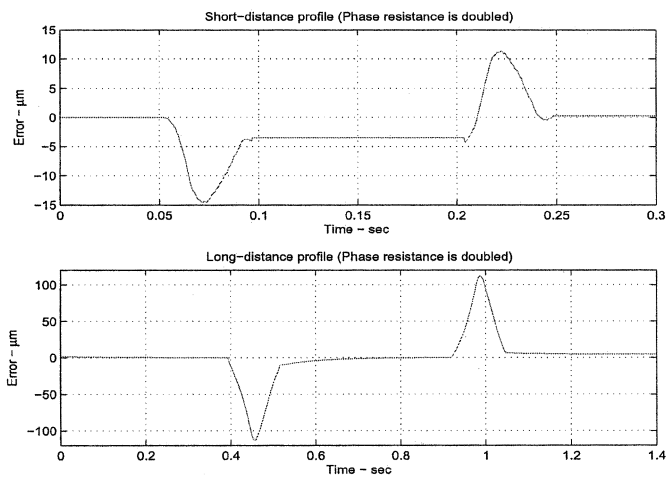


Fig. 31. Position error plot when the phase resistance is doubled.

TABLE VI
FINALIZED MOTION SPECIFICATIONS

Max loading	4.6kg
Max acceleration/deceleration	2.5g
Max velocity	1ms ⁻¹
Max Steady state error	3.5 μ m

Finally, in order to further test the robustness of the proposed lookup table force linearization scheme and the proposed plug-in robust compensator, the phase resistance of the motor windings is artificially doubled using external resistors connected in series of the original motor windings. The two designed position profiles are tracked again and the results are shown in Fig. 31. The position error of the short-distance profile is almost not affected because the peak current requirement for this profile is only 1 A. Therefore, double the phase resistance value (3.2 Ω) does not deteriorate the current tracking performance for this particular application due to the high dc-link voltage (150 V). However, the dynamic error of the long-distance profile does increase from 100 to 110 μ m when the phase resistance is doubled. This is expected as the peak current requirement for this profile is around 11 A and the increase in phase resistance will reduce the current loop tracking bandwidth while delivering high output current. The end result is the increase in dynamic tracking error when accurate high-output current tracking is required.

In summary, with the help of the plug-in robust compensator, the proposed LSRM can achieve high-performance motions for different-distance position profile tracking. The application of LSRMs in micrometer position control applications is definitely valuable to the high-precision manufacturing industry. In short, the final motion specifications with the help of the plug-in compensator are summarized in Table VI.

V. CONCLUSION

In this paper the design, manufacture, and verification of an LSRM for precision position control application were discussed. A current–force–position lookup table, based on the

experimental data, is developed to perform the force linearization in the LSRM system. The proposed motor controller can be implemented using low-cost microcontrollers/DSPs as the control algorithm established in this paper does not involve any complex mathematical function such as sine, cosine, and square root functions. In addition, the 21 \times 21 small-size lookup table can also be implemented efficiently with a small memory space.

The simple 2DOF PD position controller with the lookup table force linearization scheme can achieve satisfactory output performance for long-distance position profiles. However, the transient tracking response for short-distance position profiles should be further improved. A plug-in robust compensator using the \mathcal{H}_∞ loop-shaping design technique is employed to improve the system robustness. The novel plug-in feature of the proposed compensator can coexist with the existing 2DOF controller and does not affect the overall system stability. All-distance position profiles can be tracked accurately with the addition of the plug-in robust compensator, and the output performance for all designed profiles satisfies the design specifications.

The LSRM system can be further explored using a large-current-rating amplifier, but the heating problem should be considered for long-time running. In addition, the cost of the LSRM system can further be reduced using a novel low-cost sensor based on the unique open motor structure [21] or sensorless control.

The application of LSRMs for micrometer position control is valuable in the high-precision manufacturing industry. In the past, LSRMs were always used only in velocity control applications such as transportation vehicles. The development of accurate position control for LSRMs can definitely increase the popularity of their applications. In conclusion, the switched reluctance linear motion system described in this paper is robust, reliable, and needs few mechanical adjustments. Owing to its good performance and low manufacturing cost, the actuator can be applied to many new and high-end applications which require high-precision and high-speed motions. It will also have a tendency to replace many traditional X–Y tables that operate by rotary motors and mechanical lead screws.

REFERENCES

- [1] T. J. E. Miller, *Switched Reluctance Motor and Their Control*. London, U.K.: Oxford Univ. Press, 1993.
- [2] P. C. Kjaer, J. J. Gribble, and T. J. E. Miller, “High-grade control of switched reluctance machines,” *IEEE Trans. Ind. Electron.*, vol. 33, pp. 1585–1593, Dec. 1997.
- [3] D. M. Dawson, J. Hu, and T. C. Burg, *Nonlinear Control of Electric Machinery*. New York: Marcel Dekker, 1998.
- [4] I. Boldea and S. A. Nasar, *Linear Electric Actuators and Generators*. Cambridge, U.K.: Cambridge Univ. Press, 1997.
- [5] C. T. Liu and J. L. Kuo, “Experimental investigation and 3-D modeling of linear variable-reluctance machine with magnetic-flux decoupled windings,” *IEEE Trans. Magn.*, vol. 30, pp. 4737–4739, Nov. 1994.
- [6] C. T. Liu, L. F. Chen, J. L. Kuo, Y. N. Chen, Y. J. Lee, and C. T. Leu, “Microcomputer control implementation of transverse flux linear switched reluctance machine with rule-based compensator,” *IEEE Trans. Energy Conversion*, vol. 11, pp. 70–75, Mar. 1996.
- [7] H. K. Bae, B. S. Lee, P. Vijayraghavan, and R. Krishnan, “A linear switched reluctance motor: converter and control,” *IEEE Trans. Ind. Appl.*, vol. 36, pp. 1351–1359, Sept./Oct. 2000.
- [8] B. S. Lee, H. K. Bae, P. Vijayraghavan, and R. Krishnan, “Design of a linear switched reluctance machine,” *IEEE Trans. Ind. Appl.*, vol. 36, pp. 1571–1580, Nov./Dec. 2000.

- [9] J. Lucidarme, A. Amouri, and M. Poloujadoff, "Optimum design of longitudinal field variable reluctance motors-application to a high performance actuator," *IEEE Trans. Energy Conversion*, vol. 8, pp. 357–361, Sept. 1993.
- [10] U. S. Deshpande, J. J. Cathey, and E. Richter, "A high force density linear switched reluctance machine," in *Conf. Rec. IEEE-IAS Annu. Meeting*, vol. 1, Oct. 1993, pp. 251–257.
- [11] J. Corda and E. Skopljak, "Linear switched reluctance actuator," in *Proc. 6th Int. Conf. Electrical Machines and Drives*, Saint Nazaire, France, Sept. 1993, pp. 535–539.
- [12] M. F. Rahman, N. C. Cheung, and K. W. Lim, "Modeling of a nonlinear solenoid toward the development of a proportional actuator," in *Proc. 5th Int. Conf. Modeling and Simulation of Electrical Machines, Convertors and Systems, ELECTRIMACS'96*, vol. 2, Saint Nazaire, France, Sept. 1996, pp. 695–670.
- [13] —, "Converting a switching solenoid to a proportional actuator," *Trans. Inst. Elect. Eng. Jpn.*, pt. D, vol. I-16, no. 5, pp. 531–537, May 1996.
- [14] P. P. Khargonekar and K. R. Poolla, "Uniformly optimal control of linear time-invariant plants: nonlinear time-varying controllers," *Syst. Control Lett.*, vol. 6, no. 5, pp. 303–308, 1986.
- [15] D. C. McFarlane and K. Glover, *Robust Controller Design Using Normalized Coprime Factor Plant Descriptions*. Berlin, Germany: Springer-Verlag, 1990.
- [16] G. J. Balas, J. C. Doyle, K. Glover, A. Packard, and R. Smith, *μ -Analysis and Synthesis Toolbox*. Natick, MA: The MathWorks Inc., 1994.
- [17] M. Vidyasagar, *Control System Synthesis*. Cambridge, MA: MIT Press, 1985.
- [18] K. Zhou and Z. Ren, "A new controller architecture for high performance, robust, adaptive, and fault tolerant control," *IEEE Trans. Automat. Contr.*, vol. 46, pp. 1613–1618, Oct. 2000.
- [19] W. C. Gan and L. Qiu, "Design and analysis of a plug-in robust compensator: an application to indirect-field-oriented-control induction machine drives," *IEEE Trans. Ind. Electron.*, vol. 50, pp. 272–282, Apr. 2003.
- [20] W. C. Gan and N. C. Cheung, "Design of a linear switched reluctance motor for high precision applications," in *Proc. 3rd IEEE Int. Electric Machines and Drives Conf.*, June 2001, pp. 701–704.
- [21] —, "A low-cost linear switched reluctance motor with integrated position sensor for general-purpose three-phase motor controllers," in *Proc. 27th Annu. Conf. IEEE Industrial Electronics Society*, Dec. 2001, pp. 468–473.



Wai-Chuen Gan (S'94–M'02) received the B.Eng. degree in electronic engineering, and the M.Phil. and Ph.D. degrees in electrical and electronic engineering, with first class honors and academic achievement award, from The Hong Kong University of Science and Technology, Hong Kong, in 1995, 1997, and 2001, respectively.

From 1997 to 1999, he was with ASM Assembly Automation HK Ltd., Hong Kong, as a Motion Control Application Engineer. From 2000 to 2001, he was a Research Assistant in the Department of the Electrical Engineering, The Hong Kong Polytechnic University. In 2002, he rejoined ASM Assembly Automation HK Ltd., where he is responsible for the development of analog and digital motor drivers. His current research interests include robust control of ac machines, power electronics, design and control of linear switched reluctance motors, and control of stepping motors via interconnection and damping assignment.



Norbert C. Cheung (S'95–M'97) received the B.Sc. degree from the University of London, London, U.K., in 1981, the M.Sc. degree from the University of Hong Kong, Hong Kong, in 1987, and the Ph.D. degree from the University of New South Wales, Sydney, Australia, in 1995.

From 1981 to 1985, he was an Electronic Engineer working in industry in the areas of servo drives and industrial electronics. During this period, he was the Project Leader for the development of Hong Kong's first Photoplotter System, a high-precision CNC light plotting machine for PCB production. From 1985 to 1992, he was a Lecturer/Senior Lecturer in the Department of Electrical Engineering, The Hong Kong Polytechnic University, Hong Kong. Following his Ph.D. studies, he was with ASM Assembly Automation Ltd. for two years, working in the areas of intelligent motion control and robotic systems for semiconductor manufacturing. He then rejoined The Hong Kong Polytechnic University, where he is currently a Lecturer in the Electrical Engineering Department. His research interests are motion control systems, actuators design, and motor drives.



Li Qiu (S'85–M'90–SM'98) received the B.Eng. degree from Hunan University, Changsha, China, in 1981, and the M.A.Sc. and Ph.D. degrees in electrical engineering from the University of Toronto, Toronto, ON, Canada, in 1987 and 1990, respectively, all in electrical engineering.

In 1993, he joined the Department of Electrical and Electronic Engineering, Hong Kong University of Science and Technology, Hong Kong, as an Assistant Professor. He is currently an Associate Professor. He has also held research and teaching positions at the University of Toronto, Canadian Space Agency, University of Waterloo, University of Minnesota, Zhejiang University, and Australia Defence Force Academy. His current research interests include systems control theory, signal processing, and motor control.

Dr. Qiu served as an Associate Editor of the IEEE TRANSACTIONS ON AUTOMATIC CONTROL and *Automatica*.